Chemical Science

EDGE ARTICLE

View Article Online
View Journal | View Issue

Cite this: *Chem. Sci.*, 2017, **8**, 541

Photodriven hydrogen evolution by molecular catalysts using Al_2O_3-protected perylene-3,4-dicarboximide on NiO electrodes†

Rebecca J. Kamire, Marek B. Majewski, William L. Hoffeditz, Brian T. Phelan, Omar K. Farha, Joseph T. Hupp and Michael R. Wasielewski*

The design of efficient hydrogen-evolving photocathodes for dye-sensitized photoelectrochemical cells (DSPECs) requires the incorporation of molecular light absorbing chromophores that are capable of delivering reducing equivalents to molecular proton reduction catalysts at rates exceeding those of charge recombination events. Here, we report the functionalization and kinetic analysis of a nanostructured NiO electrode with a modified perylene-3,4-dicarboximide chromophore (**PMI**) that is stabilized against degradation by atomic layer deposition (ALD) of thick insulating Al_2O_3 layers. Following photoinduced charge injection into NiO in high yield, films with Al_2O_3 layers demonstrate longer charge separated lifetimes as characterized *via* femtosecond transient absorption spectroscopy and photoelectrochemical techniques. The photoelectrochemical behavior of the electrodes in the presence of Co(II) and Ni(II) molecular proton reduction catalysts is examined, revealing reduction of both catalysts. Under prolonged irradiation, evolved H_2 is directly observed by gas chromatography supporting the applicability of **PMI** embedded in Al_2O_3 as a photocathode architecture in DSPECs.

Received 5th June 2016
Accepted 17th August 2016

DOI: 10.1039/c6sc02477g

www.rsc.org/chemicalscience

Introduction

The harvesting and storage of light energy in the chemical bonds of liquid and gaseous fuels has been of increasing interest in recent years.[1–3] One of many promising approaches uses pairs of dye-sensitized electrodes within photoelectrochemical cells (DSPECs) to drive molecular catalysts to perform the two half reactions of water oxidation and hydrogen evolution.[4–6] Incorporation of both light-driven reactions into one efficient system presents many challenges and opportunities to understand photodriven electron transfer events, charge accumulation steps, catalytic mechanisms, and avoidance of degradation pathways within the components of DSPECs. Several designs that are capable of photodriven (or photoassisted) hydrogen evolution combine molecular catalysts with photosensitized nanomaterials in solution,[7–11] or photosensitized electrodes,[12–18] or use semiconductors as light absorbers.[19–27] Mechanistic investigation of dye-sensitized photocathode architectures remains particularly rare,[28] and such work could lead to improvement in the performance of devices. Current device designs suffer from degradation of the molecular light absorbers over time and losses in efficiency due to charge recombination at rates competitive with charge accumulation and catalysis. New chromophores based on earth abundant elements are also desirable, since the molecular photosensitizers used in the aforementioned device architectures are almost exclusively ruthenium-based, with the exception of only a few organic chromophores.[13,15,29]

We previously demonstrated that a perylene-3,4-dicarboximide (PMI) chromophore (**PMI**, Fig. 1) is capable of electron injection into nanostructured TiO_2 following photoexcitation and further capable of oxidizing a molecular water oxidation precatalyst.[30] Studies have also demonstrated the utility of **PMI**-based chromophores for photodriven hole injection into NiO in p-type dye-sensitized solar cells (DSCs),[31–36] which is encouraging for future work on hydrogen evolving photocathodes. One report suggests that no molecular catalyst is necessary for photodriven hydrogen evolution by a chromophore that includes a **PMI** moiety on NiO at pH 7,[37] and a similar **PMI**-based chromophore has driven hydrogen evolution by a cubane molybdenum-sulfide cluster in acidic conditions.[29] However, these photosensitizer designs generally require complex synthesis in order to incorporate a donor–acceptor character that extends the lifetime of the charge separated state. **PMI** can be synthesized from commercially available perylene-3,4:9,10-tetracarboxydianhydride in only four steps, and the monoanhydride opens to form the dicarboxylate when exposed to metal oxide semiconductors for convenient electrode functionalization.[30]

Department of Chemistry and Argonne-Northwestern Solar Energy Research (ANSER) Center, Northwestern University, Evanston, IL 60208-3113, USA. E-mail: m-wasielewski@northwestern.edu

† Electronic supplementary information (ESI) available: Experimental details; additional electrochemical and photoelectrochemical characterization, UV-Vis spectra, and fsTA results; quantification of evolved hydrogen; and DFT-computed ground state structure of **PMI diester**. See DOI: 10.1039/c6sc02477g

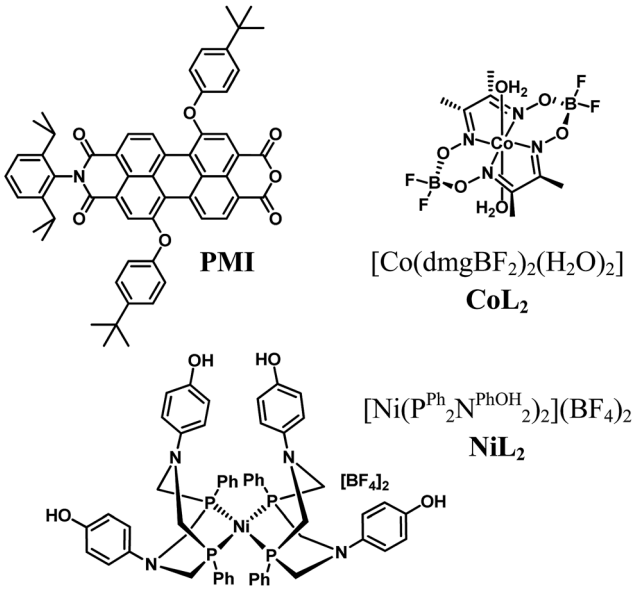

Fig. 1 Chemical structures of the **PMI** photosensitizer and the H_2 evolution catalysts.

The application of an Al_2O_3 tunneling barrier by atomic layer deposition (ALD) before dye loading on a surface has been shown to act as an alternative to complex molecular synthesis by providing the important advantages of slowing back electron transfer between charges in semiconductors and on chromophores and redox shuttles in DSCs.[16,38–46] In DSPECs, slowing charge recombination at the interface is similarly advantageous for efficient charge accumulation and catalysis. We investigate here the use of an ALD layer of varying thickness deposited after dye loading to slow charge recombination between charges in the dye and semiconductor with those on the catalyst.

However, ALD can also serve an additional purpose important in DSPECs. Dye desorption and degradation limit the performance of electrodes fabricated with **PMI**, since desorption in the acidic operating conditions and oxidative or reductive degradation of organic chromophores under catalytic conditions are some of the most significant limiting factors in the stability of DSPECs.[3,5] We and others have demonstrated that ALD of either TiO_2 or Al_2O_3 following dye absorption on nanostructured semiconductors can prevent desorption of bound molecules from surfaces in DSCs[44,47–50] and electrodes for water oxidation.[51,52] In addition, we hypothesize that a thicker layer of metal oxide surrounding the **PMI** molecules can protect the dyes from undesirable degradation side reactions. Meyer and coworkers have recently observed such a stabilization effect by Al_2O_3 ALD layers over Ru-based dyes and water oxidation catalysts on nanostructured semiconductors.[53]

Here we report the ability of **PMI** bound to nanostructured NiO electrodes and protected by Al_2O_3 to drive well-characterized cobaloxime[54,55] and $[Ni(P^R{}_2N^R{}_2)_2]^{2+}$ (ref. 56 and 57) hydrogen evolution electrocatalysts (Fig. 1). Besides their efficacy in other photodriven systems, these catalysts were selected based on their electrocatalytic hydrogen production at comparable redox potentials (Table 1, Fig. S4†). We explore the charge transfer dynamics and find that the Al_2O_3 layers not only stabilize the organic chromophores against desorption and degradation but also favor longer charge separated state lifetimes and light-driven hydrogen evolution.

Table 1 Steady-state optical properties and redox potentials (V *vs.* Ag/AgCl)

	E^{00} (eV)	$[H_2SO_4]$ (M)	E_{ox} (V)	E_{red1} (V)	E_{red2} (V)
PMI[a]	2.30	0.00	1.34	−0.79	−1.05
NiL$_2$[b]	—	0.00	—	−0.47	−0.74
	—	0.07	—	—	−0.45[c]
CoL$_2$[b]	—	0.00	—	−0.51	—
	—	0.10	—	−0.49	−0.85[c]

[a] Measurements on **PMI diester** in CH_2Cl_2 for optical expts; in 0.1 M $TBAPF_6$ in CH_3CN for redox expts.[28] [b] 1.0 mM Fc, 0.1 M Na_2SO_4 in 1 : 1 H_2O : MeCN, $[H_2SO_4]$ listed (Fig. S4). [c] Catalytic onset, as the intersection of the line of the catalytic slope with the cyclic voltammogram trace before acid addition.

Experimental

Synthesis and film preparation

The **PMI** dye and **PMI diester** (see structure in ESI†),[30] cobaloxime catalyst,[58] and nickel catalyst[57] were prepared following reported procedures. Nanostructured NiO films on conductive fluorine doped tin oxide (FTO) slides were prepared based on a literature procedure[59] and stored in a 110 °C oven until dye loading. To dye functionalize, films were gently shaken in a 0.45 mM solution of **PMI** in 1 : 3 toluene : methanol protected from light overnight, rinsed with CH_2Cl_2, and dried under a nitrogen stream. The NiO|**PMI** surface was then treated with 0–30 ALD cycles of dimethylaluminum isopropoxide and water to yield NiO|**PMI**|Al_2O_3 films, as described in the ESI.† Films for femtosecond transient absorption (fsTA) spectroscopy were either sealed under nitrogen with glass slides using UV-curable epoxy in a glove box, or placed in an acidic electrolyte solution of 0.1 M H_2SO_4 and 0.1 M Na_2SO_4 in 1 : 1 H_2O : MeCN in gas-tight cuvettes and purged with argon. The films for photoelectrochemical experiments were attached to stranded conductive wire using conductive silver epoxy (CircuitWorks Chemtronics), which was then covered with non-conductive epoxy (LOCTITE 9340 Hysol) and cured at 110 °C for 10 min.

Optical spectroscopy

Femtosecond transient absorption (fsTA) spectroscopy experiments were conducted using a regeneratively amplified Ti : sapphire laser system with samples translated in two dimensions and irradiated at 495 nm as previously described.[30,60] Further details and the fitting procedures are provided in the ESI.†

Electrochemical and photoelectrochemical experiments

Electrochemical measurements were performed using a CH Instruments Model 660A or 750E electrochemical workstation.

Measurements on the dye-functionalized films employed the films as the working electrode, a 3.0 mm diameter glassy carbon counter electrode, and an Ag/AgCl (3 M NaCl) reference electrode. Light was applied from two white LEDs (100 mW cm^{-2} incident on the sample per LED) covered with 410 nm long-pass filters. Photocatalysis experiments were performed in a sealed cell under argon with a −0.40 V bias applied concurrently with illumination for two hours. The H_2 in the headspace was identified following triplicate injections of 300 μL each into a gas chromatograph. Faradaic efficiencies were calculated from the amount of H_2 in the headspace and the amount of current passed during the experiment.

Results and discussion

Steady-state spectroscopy

The films were characterized by UV-Vis spectroscopy to gain information on the physical effect of ALD on the dye molecules (Fig. 2). The absorption spectrum for NiO|**PMI** films without ALD displays a (0,0) vibronic absorption maximum at 506 nm, a (0,1) band at 485 nm, and a small shoulder around 575 nm. The low energy shoulder is suggestive of dye aggregation[45,61] but is absent after ALD is applied. Thus, we postulate that aggregates should not play a significant role in the photophysics of the ALD-treated films. As the number of cycles of ALD is increased, the signal broadens until by 30 cycles the vibronic structure is no longer distinct and the λ_{max} is red-shifted to 522 nm. Increasing to 40 and 50 cycles produces no further spectral change (Fig. S1†). This spectrum is identical to that of the corresponding **PMI diester** spin coated onto glass but not to that of **PMI diester** encapsulated in a soft and flexible PMMA matrix (Fig. S2†), which suggests that the change in band shape after ALD could be due to the imposition of structural rigidity on **PMI** enforced by the surrounding Al_2O_3. The red-shift is likely due to an untwisting of the **PMI** core that is twisted in the free molecule by the presence of the bulky phenoxy groups.[61] It is unlikely that the shift results from a change in dielectric environment, as we have not observed that effect in previous work.[45,47]

In an attempt to predict the Al_2O_3 thickness with respect to the **PMI** molecules, the geometry optimized **PMI diester** structure was obtained from DFT calculations (B3LYP/6-31G*) and shows that the maximum height of **PMI** from the NiO surface cannot be more than 17.5 Å (Fig. S23 and Table S3†). The ALD growth rate on flat surfaces is *ca.* 1 Å per cycle as determined by ellipsometry, so it was initially anticipated that the Al_2O_3 layer would fully encapsulate **PMI** by 20 cycles of ALD. However, we surmise based on the change in band shapes in the absorption spectra between 20 and 30 cycles of ALD, and no further changes thereafter, that only by 30 cycles of ALD is the dye molecule effectively encapsulated in Al_2O_3.

The stability of the dye molecules on the surface was also investigated by UV-Vis spectroscopy after the ALD process and after exposure to ambient light and air over 45 days (Fig. S3†). Minimal dye degradation was observed during the ALD treatment, based on the change in shape of the absorption curves, but following ALD, dye degradation does occur over time. Degradation decreases with increasing Al_2O_3 thickness so that by 30 cycles degradation is negligible over the 45 day period investigated, which is promising for use of ALD-treated NiO|dye films in devices and further supports the assertion that 30 cycles of ALD is sufficient to cover **PMI**.

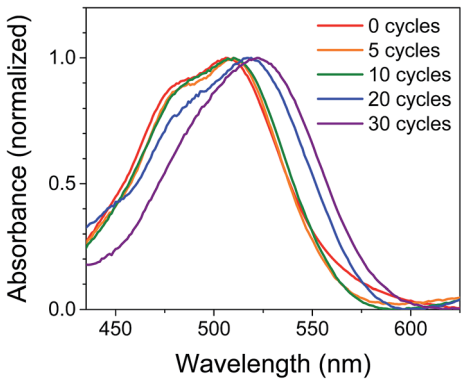

Fig. 2 Normalized UV-Vis absorption spectra of NiO|**PMI** films treated with 0–30 cycles of Al_2O_3 ALD. The NiO background is subtracted.

Electrochemistry

In order to examine the energetic driving force for the desired photodriven charge transfer steps, we compare the redox properties of **PMI** as determined in our previous work with those of the catalysts and with the NiO valence band (Table 1).[30] The NiO valence band is sufficiently low in energy that it is accessible for hole injection from **PMI** even at low pH (0.52 V *vs.* Ag/AgCl),[12,62,63] and fast hole injection from similar **PMI**-based chromophores has been observed previously.[64] The first reduction potentials, which are reversible in the absence of acid and semi-reversible in its presence, and the onsets of catalysis for $\mathbf{NiL_2}$ and $\mathbf{CoL_2}$ were measured by cyclic voltammetry and are reported in Fig. S4† and summarized in Table 1. The first reduction potential of **PMI**, E_{red} = −0.79 V *vs.* Ag/AgCl, is sufficiently negative to reduce either catalyst by one electron. In the presence of 0.1 M H_2SO_4, the catalytic onset for $\mathbf{NiL_2}$ is milder than the first reduction without acid, so **PMI** should be able to initiate catalysis. The $\mathbf{CoL_2}$ catalyst, however, has a catalytic onset of −0.85 V *vs.* Ag/AgCl, so catalysis without applied bias, if possible, is expected to be less efficient than for $\mathbf{NiL_2}$.

Transient absorption spectroscopy

We have previously reported the fsTA spectroscopic characterization of the excited state decay of the singlet excited state of **PMI** (^{1}***PMI**) on Al_2O_3, where neither electron nor hole injection into the semiconductor is energetically accessible.[30] The ^{1}***PMI** state that is formed upon excitation of Al_2O_3|**PMI** (dry) films is characterized by a ground state bleach and stimulated emission signal at 440 to 600 nm and an excited state absorption with a maximum centered at 675 nm (species A, Fig. S7A†). The subsequent decay of ^{1}***PMI** along a number of pathways including excimer formation[65] is approximated using a species-associated model in which ^{1}***PMI** (species A) decays to species

B, which decays to species C, which decays to the ground state (GS). While the spectra for "species B" and "species C" contain contributions from the several species formed along these decay pathways, excimer can be identified by a loss of stimulated emission and red-shift and broadening of the absorptive signal in species C (Fig. S7A†).

NiO|**PMI** films were then studied by fsTA spectroscopy and, by comparison to the results for Al_2O_3|**PMI**, photodriven hole injection into NiO and subsequent charge recombination were identified for both dry films and films in acidic solution (Fig. 3 and S6–S9†). The lack of significant stimulated emission and excimer signal in the time-resolved spectra for all NiO|**PMI** samples indicates that nearly quantitative hole injection into NiO occurs very rapidly. The ^{1}***PMI** spectra (Fig. 3B, species A) and rate of hole injection were identified by global fitting to an A → B → C → D → GS model, where hole injection (A → B) fits to ~0.5 ps for all samples and is likely multiexponential with an

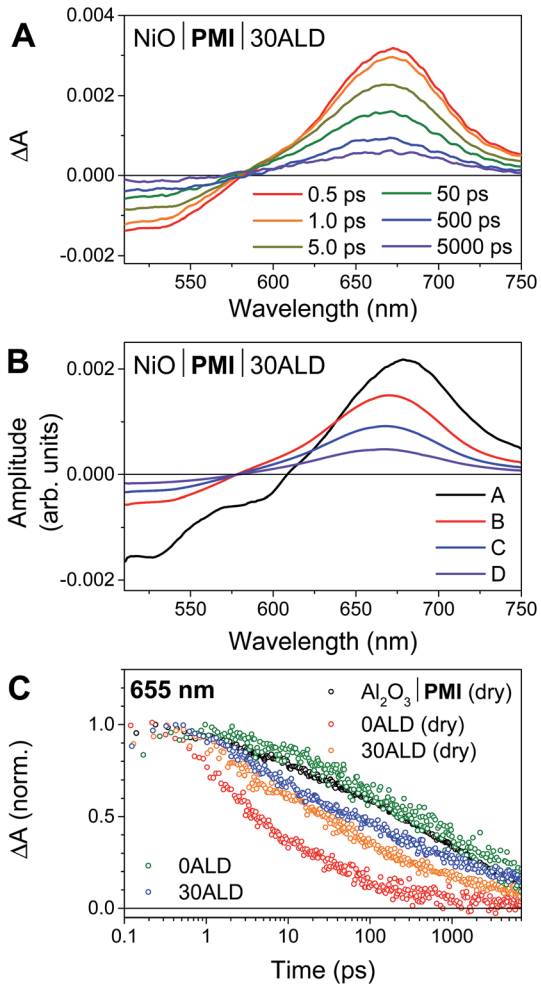

Fig. 3 (A) fsTA spectra of NiO|**PMI**|30ALD in 0.1 M H_2SO_4 + 0.1 M Na_2SO_4 in 1 : 1 H_2O : MeCN under argon following excitation with a 495 nm laser pulse. (B) Species-associated spectra obtained by a global fit of the fsTA spectra to an A → B → C → D → ground state (GS) model. (C) Normalized single wavelength traces at 655 nm from fsTA results of Al_2O_3|**PMI** (black), NiO|**PMI** (red), and NiO|**PMI**|30ALD (orange) dry under nitrogen and NiO|**PMI** (green) and NiO|**PMI**|30ALD (blue) in the electrolyte conditions as above.

even faster component occurring within the instrument response time (Table S1†).

For the NiO|**PMI** (dry) film, an excimer population is observed spectrally as a shoulder at 560–600 nm in species B–D (Fig. S9†) and kinetically as a fast rate of decay at 655 nm (Fig. 3C). The shape of the 0.5 ps spectrum for the film without ALD, with a very blue-shifted *x*-intercept of about 575 nm, indicates that the excimer population is large and begins to form within the instrument response time. The A → B lifetime of 0.6 ± 0.3 ps is not significantly different from the A → B lifetimes for the other samples, so excimer formation likely occurs on a similar timescale and competitively with hole injection. Given the large driving force for hole injection from ^{1}***PMI** discussed above, it is likely that hole injection also occurs from the excimer state. A much smaller excimer population is also observed in the 500 ps and 5000 ps spectra at 550–600 nm for films without ALD under solvent conditions. The low excimer intensity in these samples likely results from dye interaction with solvent molecules weakening the interchromophore coupling. No excimer is observed for any of the films with 30 cycles of ALD, which indicates that the disaggregation induced by ALD eliminates excimer formation so that hole injection becomes the strongly dominant process.

Following hole injection, the resulting signal is characterized by a ground state bleach centered at 525 nm and an absorptive feature with a λ_{max} around 665 nm and is consistent with **PMI**$^{\bullet-}$ (Fig. 3A).[64,66] This signal decays with little change in shape as recombination with holes in NiO occurs (species B–D, Fig. 3B). Recombination is non-exponential, as expected for dye-sensitized semiconductors,[64,67] and could not be adequately fit with fewer than three rates of decay. Consequently, the resulting fit carries a large degree of uncertainty, with values varying only slightly from those used as artificial starting values when initiating the fit. A comparison of the normalized kinetic traces at 665 nm provides more meaningful information (Fig. 3C). Recombination is slowed by the presence of the acidic solution for films with 0ALD, as the **PMI** molecules experience a more polar environment in solution and thus a lower energy **PMI**$^{\bullet-}$ state.[68] This finding agrees with a previous study that found **PMI**-sensitized NiO to lie in the Marcus normal region.[64] Thus, dye molecules encased in Al_2O_3, which experience an environment of intermediate polarity, display recombination rates between those for 0ALD films with and without solution present. Recombination is only minimally impeded by solution for films with 30ALD because the polarity of the dye environment remains unchanged. This finding indicates that the ALD layer should also shield **PMI** from catalyst molecules in solution, and slow charge recombination between the reduced catalyst and the surface, as long as the layer is thin enough for initial electron transfer through the layer to the catalyst to occur. However, catalyst reduction could not be directly identified from the fsTA experiments because samples with either $\mathbf{NiL_2}$ or $\mathbf{CoL_2}$ in solution had indistinguishable rates of decay from samples without catalyst (Fig. S10†). We conclude that, while **PMI** successfully injects holes into NiO in high yield and ALD favors injection over excimer formation, the majority of the electrons on **PMI** molecules recombine with holes in NiO before

catalyst diffusion to the surface and subsequent catalyst reduction can occur. All reported photocathodes based on sensitized NiO, including those with surface-bound catalyst, are similarly limited by fast recombination.[12–18,28] We turned to photoelectrochemical techniques to probe the fate of any charge separated states that are sufficiently long-lived to drive photocatalysis.

Photoelectrochemistry: evidence of hydrogen evolution

Following confirmation that the desired hole injection occurs from **PMI** into NiO, photoelectrochemical techniques were used to probe the ability of **PMI** to reduce **NiL$_2$** and **CoL$_2$** catalysts and drive hydrogen evolution. Fig. 4 displays results for linear sweep voltammetry (LSV) experiments on NiO|**PMI** with 30 cycles of Al_2O_3 ALD (NiO|**PMI**|30ALD) in an acidic 1 : 1 H_2O : MeCN solution (5 mV s^{-1} from 0.00 to −0.55 V, 10 s light on/off cycles). In the absence of **PMI**, photocurrent is negligible (blue), but when **PMI** is present, the photocurrent is enhanced (black). When the light is turned on, an initial strong photocurrent that rapidly decays results from reduction of the **PMI** molecules on the surface and local capacitance effects[53] and hole injection that is more rapid than dye regeneration.[69] It is followed by a plateau where hole injection and dye regeneration are in equilibrium. With either **NiL$_2$** or **CoL$_2$** but without acid, the photocurrent is enhanced in a wave-like feature around the first reduction of each catalyst (−0.3 to −0.5 V) (Fig. S11 and S12†), which suggests that photoassisted catalyst reduction from **PMI** occurs. Upon addition of both acid and 0.5 mM **NiL$_2$** or 0.5 mM **CoL$_2$** to the solution (Fig. 4, red), the photocurrent traces are not simply the sum of those observed for the films with only H_2SO_4 and those with only catalyst. Instead, the films display a further enhanced photocurrent that increases at increasingly negative potentials and lacks capacitive features. The stronger photocurrent at more negative biases reflects the higher yield of reduced catalyst resulting from slowed hole recombination at these potentials. The lack of capacitive features indicates that **PMI** is rapidly regenerated by the catalyst following hole injection into NiO at any applied potential within the range. These changes together indicate that the second reduction of each catalyst and subsequent turnover to produce hydrogen occur.[12,53,69]

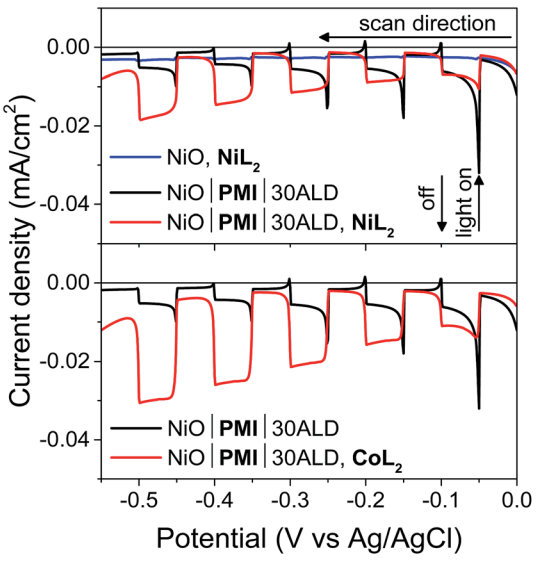

Fig. 4 Linear sweep voltammetry measurements with 10 s light on/off cycles on a NiO working electrode with 0.5 mM **NiL$_2$** (blue) and on a single NiO|**PMI**|30ALD working electrode without catalyst (black) and with 0.5 mM **NiL$_2$** or 0.5 mM **CoL$_2$** (red) (conditions: 0.1 M H_2SO_4 and 0.1 M Na_2SO_4 in 1 : 1 H_2O : MeCN, 5 mV s^{-1}).

Films with 0–20 cycles of Al_2O_3 ALD and either catalyst also display characteristics of proton reduction for experiments run on duplicate batches of films (Fig. S13–S15†). The shapes of the photocurrent responses for films exposed to either catalyst display no sharp capacitive peak when the light is turned on and higher intensity at more negative bias as observed for the films with 30 cycles of ALD. Some of the films, however, displayed a decrease in absolute photocurrent density in the presence of catalyst relative to those without. The experiments without and with catalyst were performed consecutively on the same films for ease of comparison. Dye degradation and/or desorption at strongly negative potentials,[70] such as those used in the LSV experiments, result in less photocurrent on the second sweep for most films even without catalyst addition (data not shown). In contrast, films that have only been exposed to a −0.40 *vs.* Ag/AgCl bias, even with catalyst, do not display the photocurrent loss because the **PMI** molecules are much more stable at these mild potentials (Fig. 6B, S15 and S16†). Gratifyingly, photocurrent is stable over a 10 minute experiment for NiO|**PMI**|0–30ALD films with either catalyst at this potential (Fig. S19†). Alternatively, degradation at more negative potentials decreases as we increase the number of cycles of Al_2O_3. The color of the 30ALD films is preserved throughout the LSV experiment, unlike films with fewer ALD layers, and the photocurrent density on the second sweep is higher relative to the first sweep with increasing ALD layers (Fig. S13†). Thus, we postulate that the shapes of the photocurrent traces suggest successful hydrogen evolution occurs despite a lack of enhanced photocurrent in the presence of catalyst in some instances, and the loss of photocurrent due to degradation can be avoided on our experimental timescale by applying mild potentials and by applying sufficient Al_2O_3 coverage by ALD. We note that Meyer *et al.* have also observed a decrease in absolute photocurrent for their TiO_2|dye|ALD|catalyst|ALD samples but were able to assign a change in photocurrent signal shape to an enhanced rate of oxidative catalysis.[53]

Photoelectrochemistry: analysis of rates

In light of the preceding discussion, we propose that it is most relevant to compare photocurrent response shapes to understand the differences in charge transfer dynamics between samples. These shapes are quantified using the ratio of photocurrent density at the end of a 10 s illumination period during the LSV experiment to that at the beginning ($I_{-0.10\ V}/I_{-0.05\ V}$ or $I_{\text{light off}}/I_{\text{light on}}$, Fig. 5). Small ratios for the films without catalyst reflect the strong capacitive current spike, whereas larger current ratios for catalyst-containing samples reflect less

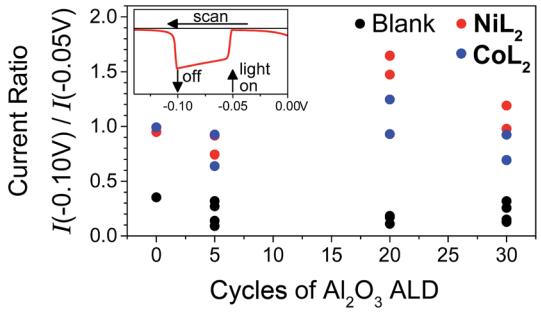

Fig. 5 Ratios of current densities at −0.10 V (light off) to those at −0.05 V (light on) during LSV in duplicate and for NiO|**PMI**|ALD films with 0–30 cycles of Al_2O_3 ALD (black, "blank") and again after additional 0.5 mM **NiL**$_2$ (red) or 0.5 mM **CoL**$_2$ (blue). The raw data for the two sets of films are reported in Fig. S13 and S15† (conditions: 0.1 M Na_2SO_4 and 0.1 M H_2SO_4 in 1 : 1 H_2O : MeCN).

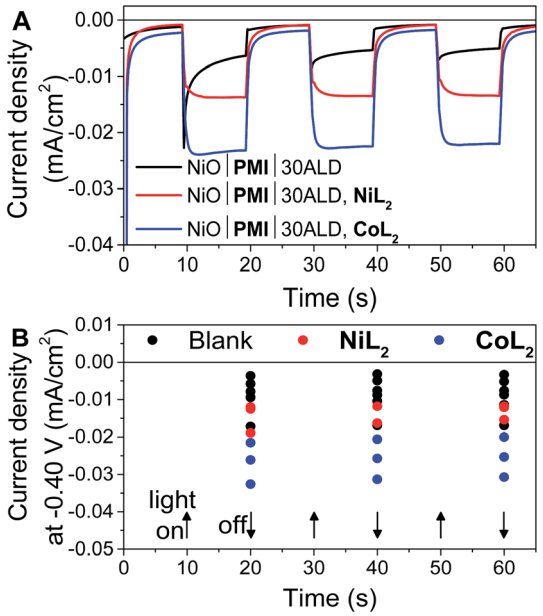

Fig. 6 (A) Current density measurements with three 10 s light on/off cycles with −0.40 V applied bias on a single NiO|**PMI**|30ALD working electrode without catalyst (black, "blank") and again after additional 0.5 mM **NiL**$_2$ (red) or 0.5 mM **CoL**$_2$ (blue). (B) Results of the same experiment with 5–30 cycles of Al_2O_3 ALD from Fig. S16.† The number of cycles of ALD is not distinguished for clarity (conditions: 0.1 M H_2SO_4 and 0.1 M Na_2SO_4 in 1 : 1 H_2O : MeCN).

decreasing or even increasing photocurrent densities during illumination. The current ratios approaching or greater than unity with catalyst indicate that rapid dye regeneration is sustained over time as the catalyst species regenerating the dye performs catalytic turnovers. Faster electron transfer to **NiL**$_2$ from the reduced dye (and slower recombination) compared to **CoL**$_2$ is evidenced by a larger current ratio $I_{-0.10\text{ V}}/I_{-0.05\text{ V}}$ for the former, likely due to the less negative catalytic onset and lower degree of reversibility of the first catalyst reduction.[12] A comparison of ratios of current densities at −0.40 V (Fig. S18†), where there is no difference in photocurrent response shape between the two catalysts, confirms that driving force is sufficiently strong and charge recombination is sufficiently slowed with the −0.40 V applied bias for the rapid second reduction of either catalyst to occur.

In potentiostatic photocurrent experiments at −0.40 V, photocurrent enhancement alone with either catalyst is a strong indicator of hydrogen evolution (Fig. 6 and S16†). The amplitude of the recorded photocurrent does not increase during the entire 10 s of illumination because a constant bias is applied throughout. In contrast to the LSV experiments discussed above, where the change in the photocurrent response shape is stronger for **NiL**$_2$ due to its milder catalytic onset potential, in these potentiostatic experiments the photocurrent enhancement with catalyst is more pronounced for **CoL**$_2$ than for **NiL**$_2$ (Fig. 6B). The higher photocurrent density for **CoL**$_2$ compared to **NiL**$_2$ may result from an easier approach of **CoL**$_2$ to the NiO|**PMI** electrode due to its less sterically bulky ligand so that catalyst reduction is faster and thus more competitive with charge recombination. Overall, however, the differences in photocurrent densities between the NiO|**PMI** electrodes with the two different catalysts are minimal compared to the differences between the catalytic currents of the two catalysts in solution driven by a glassy carbon electrode (Fig. S4†). The current densities for electrocatalysis in that case are much larger than with the photoelectrodes, which suggests that the catalyst turnover is not rate-limiting at the NiO|**PMI**|ALD electrodes. This finding emphasizes the importance of electrode design and agrees with Ji *et al.* that the shapes of the photocurrent responses observed for dye-sensitized electrodes are more dependent on the electron transfer dynamics within the electrode and between the dye and the catalyst than on the inherent kinetics of the catalysts.[16] Thus, the findings for this system should apply to systems that incorporate other catalysts as well.

The photocurrent traces also corroborate the hypothesis that hole recombination to **PMI** and to the catalyst before release of a hydrogen molecule are successfully slowed by the Al_2O_3 (ref. 69) without catastrophic losses in hole injection or catalyst reduction yields. The similar amplitude of photocurrent with the different amounts of ALD demonstrates the similar yields of charge injection and long-lived holes between samples. The effect of ALD on slowing charge transfer between the dye and the catalyst can be observed at the rise of the photocurrent traces over the initial 3 s after the light is turned on. This rise occurs as the rate of charge collection at the electrode (not necessarily the rate of charge injected into NiO) comes into equilibrium with that of charge transfer to the catalyst. With 0ALD or 5ALD and catalyst, photocurrent increases to the maximum much more slowly compared to films with more ALD (Fig. S13 and S15†). This observation is consistent with fast dye regeneration by hole transfer from the catalyst in the absence of ALD. As layers of Al_2O_3 are added, the initial maximum photocurrent is reached rapidly (followed by the slow rise with increasing potential), which indicates that dye regeneration is likely slowed by the insulating barrier. We note that permanent changes to the Al_2O_3 could contribute to the observed behavior. However, if charge transfer to the catalyst is slowed by Al_2O_3, we also expect to observe slowed recombination. An increase is

observed in the absolute photocurrent densities at the end of 10 s of illumination with increasing Al_2O_3 thickness especially in the presence of catalyst (Fig. S17†). The NiO|**PMI**|30ALD, **NiL$_2$** sample in Fig. S17† has low current density and does not match the overall trend, but a comparison with Fig. 4, 6, and S13† suggests that this film is an outlier, potentially due to poor NiO quality. These data suggest that slower recombination and longer-lived charge separated states are achieved by addition of the ALD layer, which favors catalysis. Thus, the overall effect of ALD is to slow undesirable charge recombination events without preventing forward electron transfer.

Photodriven hydrogen generation

In order to monitor the performance of the films under conditions where hydrogen was expected to form, the electrodes were held at −0.40 V under illumination for 2 h, after which evolved hydrogen was detected by gas chromatography (Fig. S20 and S21†). The applied bias, rather than detracting from the viability of the electrode design, mimics the effect of incorporating the photocathode into a tandem device with a water oxidation photoanode based on TiO_2, where the conduction band of TiO_2 is at approximately this potential.[13,15] A small but detectable amount of hydrogen was produced by films exposed to light but not to catalyst, in accordance with a report by Tong *et al.* that **PMI**-based chromophores alone can drive hydrogen evolution.[37] No hydrogen was detected for films with catalyst present in the absence of light. NiO|**PMI**|30ALD films in the presence of both catalyst and light, however, formed hydrogen with faradaic efficiencies of 98 ± 4% and 60 ± 10% for **NiL$_2$** and **CoL$_2$**, respectively (Table S2†). A lower hydrogen yield was observed for **CoL$_2$** compared to **NiL$_2$**, despite the larger photocurrents recorded for **CoL$_2$** with shorter irradiation times (Fig. 6), which is likely due to the known instability of **CoL$_2$** to hydrolysis[71] and to the overall higher activity of **NiL$_2$** under these conditions (Fig. S4†). Finally, films without ALD in the presence of **NiL$_2$** produced less hydrogen compared to those with ALD and exhibited a lower faradaic efficiency of 80 ± 10%. These films displayed a nearly complete loss of detectable **PMI** by the end of the two hour experiment, in contrast to the Al_2O_3-protected films on which **PMI** remains (Fig. S22†). This comparison reflects the improvements in stability achieved through incorporation of the Al_2O_3 layer into the electrode design.

Some high-performing electrodes resulted from variability during the preparation of the underlying NiO. One such champion NiO|**PMI**|30ALD film with **NiL$_2$** produced about four times the hydrogen with the same faradaic efficiency compared to a typical film (Fig. S20–S21 and Table S2†). From the fsTA results, it is evident that charge recombination between the hole in NiO and the electron on **PMI** occurs very rapidly and in high yield, as is common for dye-sensitized NiO devices.[12–17] The power conversion efficiency of our high-performing electrode is as a result still very low (<1%). Notably, this champion electrode did produce 1.82 ± 0.02 μmol hydrogen, which corresponds to a turnover number of about 1.5 with respect to catalyst and demonstrates that the hydrogen evolution observed here is indeed catalytic. An improved preparation of NiO, such as a recently reported treatment to passivate defect sites[72] or a single cycle of ALD before dye loading,[16] would be expected to raise the amplitude of the photocurrent response and overall performance of a device by increasing hole collection.

Conclusion

We have designed and fabricated a NiO|**PMI**|Al_2O_3 ALD photocathode architecture for photodriven hydrogen evolution that incorporates only earth-abundant elements. The **PMI** chromophores inject holes into NiO in <1 ps in high yield, and ALD of Al_2O_3 serves to disaggregate **PMI** and disfavor excimer formation as monitored by steady-state and transient optical spectroscopies. Photoelectrochemical experiments demonstrate successful photodriven reduction of and subsequent hydrogen evolution by two different molecular catalysts in solution. The Al_2O_3 layers stabilize **PMI** against desorption and degradation and slow undesirable charge recombination events so that higher photocurrent is achieved. The stabilizing effect further affords photodriven hydrogen evolution at high faradaic efficiencies. These results are promising for further exploration of ALD-embedded organic chromophores in photocathodes for photodriven hydrogen evolution. The findings that ALD of Al_2O_3 slows charge recombination and stabilizes surface-bound chromophores are expected to apply to other semiconductors that have better inherent charge recombination dynamics and to other catalysts, chromophores, and solution conditions, as long as those solution conditions are selected to allow for stability of the exposed components. Experiments are underway to attach catalysts to the electrode surface in order to improve the rate of catalyst reduction compared to recombination and better probe electron transfer dynamics between the adsorbed dye and the catalyst.

Acknowledgements

This work was supported by the Argonne-Northwestern Solar Energy Research (ANSER) Center, an Energy Frontier Research Center funded by the U.S. Department of Energy (DOE), Office of Science, Office of Basic Energy Sciences, under award number DE-SC0001059. Profilometry and ellipsometry measurements were performed in the Keck-II facility of the NU*ANCE* Center at Northwestern University, which has received support from the Soft and Hybrid Nanotechnology Experimental (SHyNE) Resource (NSF NNCI-1542205); the MRSEC program (NSF DMR-1121262) at the Materials Research Center; the International Institute for Nanotechnology (IIN); the Keck Foundation; and the State of Illinois, through the IIN. UV-Vis absorption measurements with the integrating sphere were performed in the Keck Biophysics Facility at Northwestern University, which is supported in part by grant NCI CCSG P30 CA060553 awarded to the Robert H Lurie Comprehensive Cancer Center.

References

1 N. Armaroli and V. Balzani, *Chem.–Eur. J.*, 2016, **22**, 32–57.

2 J. R. McKone, H. B. Gray and N. S. Lewis, *Chem. Mater.*, 2014, **26**, 407–414.
3 S. Berardi, S. Drouet, L. Francas, C. Gimbert-Surinach, M. Guttentag, C. Richmond, T. Stoll and A. Llobet, *Chem. Soc. Rev.*, 2014, **43**, 7501–7519.
4 Z. Yu, F. Li and L. Sun, *Energy Environ. Sci.*, 2015, **8**, 760–775.
5 H. Tian, *ChemSusChem*, 2015, **8**, 3746–3759.
6 N. Queyriaux, N. Kaeffer, A. Morozan, M. Chavarot-Kerlidou and V. Artero, *J. Photochem. Photobiol., C*, 2015, **25**, 90–105.
7 M. A. Gross, A. Reynal, J. R. Durrant and E. Reisner, *J. Am. Chem. Soc.*, 2014, **136**, 356–366.
8 F. Lakadamyali, M. Kato, N. M. Muresan and E. Reisner, *Angew. Chem., Int. Ed.*, 2012, **51**, 9381–9384.
9 F. Lakadamyali, A. Reynal, M. Kato, J. R. Durrant and E. Reisner, *Chem.–Eur. J.*, 2012, **18**, 15464–15475.
10 A. Reynal, F. Lakadamyali, M. A. Gross, E. Reisner and J. R. Durrant, *Energy Environ. Sci.*, 2013, **6**, 3291–3300.
11 S. Pullen, H. Fei, A. Orthaber, S. M. Cohen and S. Ott, *J. Am. Chem. Soc.*, 2013, **135**, 16997–17003.
12 C. E. Castillo, M. Gennari, T. Stoll, J. Fortage, A. Deronzier, M. N. Collomb, M. Sandroni, F. Legalite, E. Blart, Y. Pellegrin, C. Delacote, M. Boujtita, F. Odobel, P. Rannou and S. Sadki, *J. Phys. Chem. C*, 2015, **119**, 5806–5818.
13 L. Li, L. Duan, F. Wen, C. Li, M. Wang, A. Hagfeldt and L. Sun, *Chem. Commun.*, 2012, **48**, 988–990.
14 K. Fan, F. Li, L. Wang, Q. Daniel, E. Gabrielsson and L. Sun, *Phys. Chem. Chem. Phys.*, 2014, **16**, 25234–25240.
15 F. Li, K. Fan, B. Xu, E. Gabrielsson, Q. Daniel, L. Li and L. Sun, *J. Am. Chem. Soc.*, 2015, **137**, 9153–9159.
16 Z. Ji, M. He, Z. Huang, U. Ozkan and Y. Wu, *J. Am. Chem. Soc.*, 2013, **135**, 11696–11699.
17 C. J. Wood, G. H. Summers, C. A. Clark, N. Kaeffer, M. Braeutigam, L. R. Carbone, L. D'Amario, K. Fan, Y. Farre, S. Narbey, F. Oswald, L. A. Stevens, C. D. J. Parmenter, M. W. Fay, A. La Torre, C. E. Snape, B. Dietzek, D. Dini, L. Hammarstrom, Y. Pellegrin, F. Odobel, L. Sun, V. Artero and E. A. Gibson, *Phys. Chem. Chem. Phys.*, 2016, **18**, 10727–10738.
18 M. A. Gross, C. E. Creissen, K. L. Orchard and E. Reisner, *Chem. Sci.*, 2016, **7**, 5537–5546.
19 J. Huang, K. L. Mulfort, P. Du and L. X. Chen, *J. Am. Chem. Soc.*, 2012, **134**, 16472–16475.
20 B. C. M. Martindale, G. A. M. Hutton, C. A. Caputo and E. Reisner, *J. Am. Chem. Soc.*, 2015, **137**, 6018–6025.
21 C. A. Caputo, M. A. Gross, V. W. Lau, C. Cavazza, B. V. Lotsch and E. Reisner, *Angew. Chem., Int. Ed.*, 2014, **53**, 11538–11542.
22 C. Gimbert-Suriñach, J. Albero, T. Stoll, J. Fortage, M.-N. Collomb, A. Deronzier, E. Palomares and A. Llobet, *J. Am. Chem. Soc.*, 2014, **136**, 7655–7661.
23 Y. Xu, X. Yin, Y. Huang, P. Du and B. Zhang, *Chem.–Eur. J.*, 2015, **21**, 4571–4575.
24 P. Meng, M. Wang, Y. Yang, S. Zhang and L. Sun, *J. Mater. Chem. A*, 2015, **3**, 18852–18859.
25 Y. Chen, H. Chen and H. Tian, *Chem. Commun.*, 2015, **51**, 11508–11511.
26 A. Krawicz, D. Cedeno and G. F. Moore, *Phys. Chem. Chem. Phys.*, 2014, **16**, 15818–15824.
27 J. Seo, R. T. Pekarek and M. J. Rose, *Chem. Commun.*, 2015, **51**, 13264–13267.
28 A. M. Brown, L. J. Antila, M. Mirmohades, S. Pullen, S. Ott and L. Hammarström, *J. Am. Chem. Soc.*, 2016, **138**, 8060–8063.
29 K. A. Click, D. R. Beauchamp, Z. Huang, W. Chen and Y. Wu, *J. Am. Chem. Soc.*, 2016, **138**, 1174–1179.
30 R. J. Lindquist, B. T. Phelan, A. Reynal, E. A. Margulies, L. E. Shoer, J. R. Durrant and M. R. Wasielewski, *J. Mater. Chem. A*, 2016, **4**, 2880–2893.
31 A. Morandeira, J. Fortage, T. Edvinsson, L. Le Pleux, E. Blart, G. Boschloo, A. Hagfeldt, L. Hammarström and F. Odobel, *J. Phys. Chem. C*, 2008, **112**, 1721–1728.
32 A. Nattestad, A. J. Mozer, M. K. R. Fischer, Y. B. Cheng, A. Mishra, U. Bach and P. Bauerle, *Nat. Mater.*, 2010, **9**, 31–35.
33 L. Le Pleux, A. L. Smeigh, E. Gibson, Y. Pellegrin, E. Blart, G. Boschloo, A. Hagfeldt, L. Hammarstrom and F. Odobel, *Energy Environ. Sci.*, 2011, **4**, 2075–2084.
34 M. Weidelener, A. Mishra, A. Nattestad, S. Powar, A. J. Mozer, E. Mena-Osteritz, Y.-B. Cheng, U. Bach and P. Baeuerle, *J. Mater. Chem.*, 2012, **22**, 7366–7379.
35 J. Warnan, J. Gardner, L. Le Pleux, J. Petersson, Y. Pellegrin, E. Blart, L. Hammarstrom and F. Odobel, *J. Phys. Chem. C*, 2014, **118**, 103–113.
36 Z. Liu, D. Xiong, X. Xu, Q. Arooj, H. Wang, L. Yin, W. Li, H. Wu, Z. Zhao, W. Chen, M. Wang, F. Wang, Y.-B. Cheng and H. He, *ACS Appl. Mater. Interfaces*, 2014, **6**, 3448–3454.
37 L. Tong, A. Iwase, A. Nattestad, U. Bach, M. Weidelener, G. Gotz, A. Mishra, P. Bauerle, R. Amal, G. G. Wallace and A. J. Mozer, *Energy Environ. Sci.*, 2012, **5**, 9472–9475.
38 C. Prasittichai and J. T. Hupp, *J. Phys. Chem. Lett.*, 2010, **1**, 1611–1615.
39 M. J. DeVries, M. J. Pellin and J. T. Hupp, *Langmuir*, 2010, **26**, 9082–9087.
40 V. O. Williams, N. C. Jeong, C. Prasittichai, O. K. Farha, M. J. Pellin and J. T. Hupp, *ACS Nano*, 2012, **6**, 6185–6196.
41 C. Prasittichai, J. R. Avila, O. K. Farha and J. T. Hupp, *J. Am. Chem. Soc.*, 2013, **135**, 16328–16331.
42 M. J. Katz, M. J. D. Vermeer, O. K. Farha, M. J. Pellin and J. T. Hupp, *Langmuir*, 2013, **29**, 806–814.
43 M. J. Katz, M. J. DeVries Vermeer, O. K. Farha, M. J. Pellin and J. T. Hupp, *J. Phys. Chem. B*, 2015, **119**, 7162–7169.
44 K. Hanson, M. D. Losego, B. Kalanyan, D. L. Ashford, G. N. Parsons and T. J. Meyer, *Chem. Mater.*, 2013, **25**, 3–5.
45 H.-J. Son, C. H. Kim, D. W. Kim, N. C. Jeong, C. Prasittichai, L. Luo, J. Wu, O. K. Farha, M. R. Wasielewski and J. T. Hupp, *ACS Appl. Mater. Interfaces*, 2015, **7**, 5150–5159.
46 T. W. Hamann, O. K. Farha and J. T. Hupp, *J. Phys. Chem. C*, 2008, **112**, 19756–19764.
47 H.-J. Son, C. Prasittichai, J. E. Mondloch, L. Luo, J. Wu, D. W. Kim, O. K. Farha and J. T. Hupp, *J. Am. Chem. Soc.*, 2013, **135**, 11529–11532.
48 K. Hanson, M. D. Losego, B. Kalanyan, G. N. Parsons and T. J. Meyer, *Nano Lett.*, 2013, **13**, 4802–4809.

49 N. C. Jeong, H.-J. Son, C. Prasittichai, C. Y. Lee, R. A. Jensen, O. K. Farha and J. T. Hupp, *J. Am. Chem. Soc.*, 2012, **134**, 19820–19827.
50 H.-J. Son, X. Wang, C. Prasittichai, N. C. Jeong, T. Aaltonen, R. G. Gordon and J. T. Hupp, *J. Am. Chem. Soc.*, 2012, **134**, 9537–9540.
51 A. K. Vannucci, L. Alibabaei, M. D. Losego, J. J. Concepcion, B. Kalanyan, G. N. Parsons and T. J. Meyer, *Proc. Natl. Acad. Sci. U. S. A.*, 2013, **110**, 20918–20922.
52 L. Alibabaei, B. D. Sherman, M. R. Norris, M. K. Brennaman and T. J. Meyer, *Proc. Natl. Acad. Sci. U. S. A.*, 2015, **112**, 5899–5902.
53 A. M. Lapides, B. D. Sherman, K. Brennaman, C. J. Dares, K. R. Skinner, J. Templeton and T. J. Meyer, *Chem. Sci.*, 2015, **6**, 6398–6406.
54 P. Connolly and J. H. Espenson, *Inorg. Chem.*, 1986, **25**, 2684–2688.
55 C. Baffert, V. Artero and M. Fontecave, *Inorg. Chem.*, 2007, **46**, 1817–1824.
56 M. L. Helm, M. P. Stewart, R. M. Bullock, M. R. DuBois and D. L. DuBois, *Science*, 2011, **333**, 863–866.
57 W. A. Hoffert, J. A. S. Roberts, R. M. Bullock and M. L. Helm, *Chem. Commun.*, 2013, **49**, 7767–7769.
58 A. Bakac and J. H. Espenson, *J. Am. Chem. Soc.*, 1984, **106**, 5197–5202.
59 S. Sumikura, S. Mori, S. Shimizu, H. Usami and E. Suzuki, *J. Photochem. Photobiol., A*, 2008, **199**, 1–7.
60 R. M. Young, S. M. Dyar, J. C. Barnes, M. Juríček, J. F. Stoddart, D. T. Co and M. R. Wasielewski, *J. Phys. Chem. A*, 2013, **117**, 12438–12448.
61 Z. Chen, U. Baumeister, C. Tschierske and F. Würthner, *Chem.–Eur. J.*, 2007, **13**, 450–465.
62 J. He, H. Lindström, A. Hagfeldt and S.-E. Lindquist, *J. Phys. Chem. B*, 1999, **103**, 8940–8943.
63 G. Boschloo and A. Hagfeldt, *J. Phys. Chem. B*, 2001, **105**, 3039–3044.
64 A. L. Smeigh, L. L. Pleux, J. Fortage, Y. Pellegrin, E. Blart, F. Odobel and L. Hammarstrom, *Chem. Commun.*, 2012, **48**, 678–680.
65 M. K. Brennaman, M. R. Norris, M. K. Gish, E. M. Grumstrup, L. Alibabaei, D. L. Ashford, A. M. Lapides, J. M. Papanikolas, J. L. Templeton and T. J. Meyer, *J. Phys. Chem. Lett.*, 2015, **6**, 4736–4742.
66 M. T. Vagnini, M. W. Mara, M. R. Harpham, J. Huang, M. L. Shelby, L. X. Chen and M. R. Wasielewski, *Chem. Sci.*, 2013, **4**, 3863–3873.
67 S. Ardo and G. J. Meyer, *Chem. Soc. Rev.*, 2009, **38**, 115–164.
68 A. Weller, *J. Phys. Chem.*, 1982, **133**, 93–98.
69 D. W. Kim, S. C. Riha, E. J. DeMarco, A. B. F. Martinson, O. K. Farha and J. T. Hupp, *ACS Nano*, 2014, **8**, 12199–12207.
70 B. I. Lemon and J. T. Hupp, *J. Phys. Chem. B*, 1999, **103**, 3797–3799.
71 V. Artero, M. Chavarot-Kerlidou and M. Fontecave, *Angew. Chem., Int. Ed.*, 2011, **50**, 7238–7266.
72 C. J. Flynn, S. M. McCullough, E. Oh, L. Li, C. C. Mercado, B. H. Farnum, W. Li, C. L. Donley, W. You, A. J. Nozik, J. R. McBride, T. J. Meyer, Y. Kanai and J. F. Cahoon, *ACS Appl. Mater. Interfaces*, 2016, **8**, 4754–4761.